Measurement of Intrinsic Residual Stresses in 3D Woven Composites Using Measurement of the Displacement Fields from Hole Drilling by Electronic Speckle Pattern Interferometry and Digital Image Correlation

---

TODD S. GROSS, HILARY BUNTROCK, IGOR I. TSUKROV,
BORYS DRACH, KOSTIANTYN VASYLEVSKYI
and NICHOLAS CHAGNON

ABSTRACT

Intrinsic residual stresses in woven composites result from the coefficient of thermal expansion mismatch between the fibers and the matrix. Extrinsic residual stresses result from large scale thermal gradients during curing and cooling. Intrinsic residual stresses in 3D woven composites are sometimes severe enough to cause micro-cracking in the matrix. They are also expected to impact the fatigue resistance and the impact resistance. To the best of our knowledge, there have been no spatially resolved measurements of the intrinsic residual stress field as a function of position in the repeating weave pattern.

We used digital image correlation (DIC) and electronic speckle pattern interferometry (ESPI) to measure the surface displacement field resulting from drilling a 1 mm diameter hole at four selected locations in two different 3D woven composite architectures that represent low and high through-the-thickness constraint. The two methods are used because the displacements sometimes on the lower end of the resolution for the DIC method and the displacement gradients are sometimes too steep to resolve the fringes for the ESPI method.

Finite element models constructed with realistic fiber geometry using Dynamic Fabric Mechanic Analyzer software were utilized to estimate the residual stress field from cooling from the curing temperature. Holes were manually inserted by deactivating the elements in the hole region and the resultant displacement fields were compared to the measurements. In general, the measured displacement fields were lower in magnitude than the model predictions. In some cases, the sign of the predicted displacement field is opposite to the observed field which could be attributed to differences between the actual hole location and the hole in the model.

Todd. Gross, Hilary Buntrock, Igor Tsukrov, Kostiantyn Vasylevskyi, Nicholas Chagnon, University of New Hampshire, Department of Mechanical Engineering 33 Academic Way, Durham, NH 03824, U.S.A..
Borys Drach, New Mexico State University, Department of Mechanical and Aerospace Engineering, P.O. Box 30001, MSC 3450, Las Cruces, NM 88003-8001, U.S.A.

INTRODUCTION

The coefficient of thermal expansion mismatch between epoxy resins and carbon fibers leads to a spatially varying internal residual stress field that increases in magnitude as the composite cools from the curing temperature. This intrinsic residual stress field has periodicity corresponding to the repeating unit cell of the composite. The fibers in resin-impregnated fiber tows will generally experience compressive residual stress and the resin in the fiber tows and between the fiber tows will experience a tensile residual stress. While laminar composites can generally accommodate these residual stresses by allowing out-of-plane deformation, 3D woven composite architectures with significant through-the-thickness constraint generate large hydrostatic tensile stress in the resin between the fiber tows that leads to microcracking in the resin by void initiation.

The goal of this work is to experimentally measure the magnitude of the residual stress field in two 3D woven architectures that represent the extreme of low and high through-thickness constraint. We used digital image correlation (DIC) and electronic speckle pattern interferometry (ESPI) to measure the 2D surface displacement field that results from drilling 1 mm diameter holes at selected locations in the fiber architecture. We compared the measured 2D displacement field to the field predicted from a linear elastic 3D finite element (FE) model of the unit cell (the repeating portion of the woven composite material) for both architectures. The FE model is based on a realistic simulation of each architecture where the model was cooled from the curing temperature to room temperature assuming the stresses were zero everywhere at the curing temperature.

METHODS

Experimental Methods

Panels of 4.1 mm thickness were fabricated by Albany Engineered Composites using Hexcel RTM6 resin and Hexcel 12K IM7 PAN-based carbon fibers. The ply-to-ply architecture (shown on top in Figure 1) represented the minimum through-thickness constraint and had an overall volume fraction of 50% with in-plane unit cell dimensions of 10.16 mm by 10.16 mm. The orthogonal architecture (on bottom in Figure 1) had an overall fiber volume fraction of 55% with in-plane unit cell dimensions of 5.1 mm by 5.1 mm and represented the maximum through-thickness constraint.

Sections that contained at least nine unit cells were cut out from the panels and painted first with white, high heat spray paint. The black speckles were applied using an airbrush to get speckles that ranged in size from 5-10 μm. This was then covered with a clear matte spray paint to protect the speckles from drilling debris deposits and from removing the speckles with the water used for cooling during drilling. The sample was glued on a block mounted on a Thor Labs kinematic mount to allow precise repositioning between the before drilling and after drilling DIC images and interferograms. The same specimen was probed on both the DIC setup and the interferometry system. The apparent placement repeatability was on the order of 5 μm or less

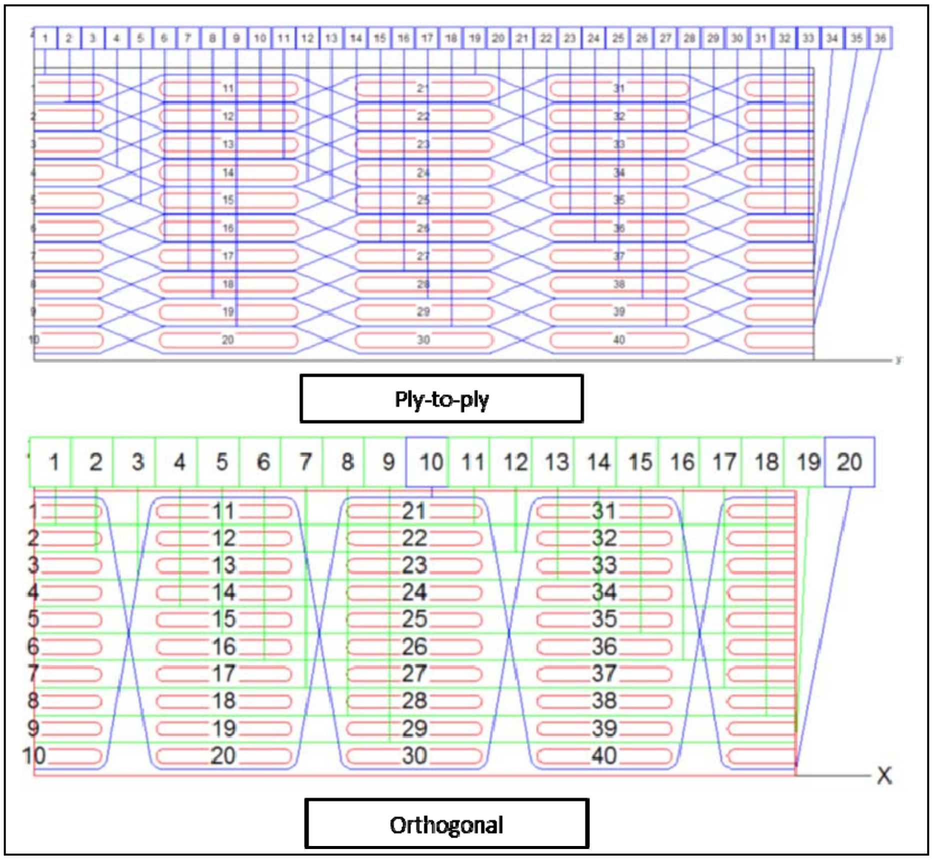

Figure 1. Ply-to-ply and orthogonal weave architectures.

Drilling the 1 mm diameter holes was accomplished with UKAM diamond coring tool. The depth was continuously measured with a dial indicator attached to the drilling head. A continuous flow of deionized water was manually applied during drilling using a squeeze bottle. The water was used to minimize the heat generated during drilling and to carry away the drilling debris. The sample was rinsed with more water after drilling and dried with a flow of warm air.

We used a VIC-Micro3D Correlated Solutions digital image correlation system to obtain before and after images to determine the in-plane displacements in the near field region around the hole. The pixel size was 3.34 µm. The typical quoted maximum resolution is 0.01 pixels. The apparent displacement noise is ~0.05 pixels which corresponds to ~0.06 µm. The sampled region was large enough so that we subtracted any tilt and displacement from re-placing the sample by performing a 2D first order, least squares fit of a 10-pixel wide region on the outer border of the image. When the apparent displacement field extended to the border, the tilt correction was only performed on the borders not impacted by the displacement field of the hole.

We used a custom-built electronic speckle pattern interferometry system similar to the one described by Diaz et al [1] to determine the in-plane displacements outside the high displacement gradient region near the hole. A diagram of the system is shown in Figure 2. We used a 50 mW Melles Griot HeNe laser that had linear polarization. The angle between the normal to the specimen and the illumination beams was 45° which results in a 448 nm displacement for a phase difference corresponding to 2π. Our system exhibited phase noise of $<\pi/25$ which corresponds to a displacement of 9 nm which is roughly 7 times lower than the DIC measurements. As for the DIC measurements, a picture frame region around the edge of the image was used to correct for any displacements from repositioning the sample on the holder. The full field image was not used for comparison to DIC images. We just used the data for a single slice through the hole.

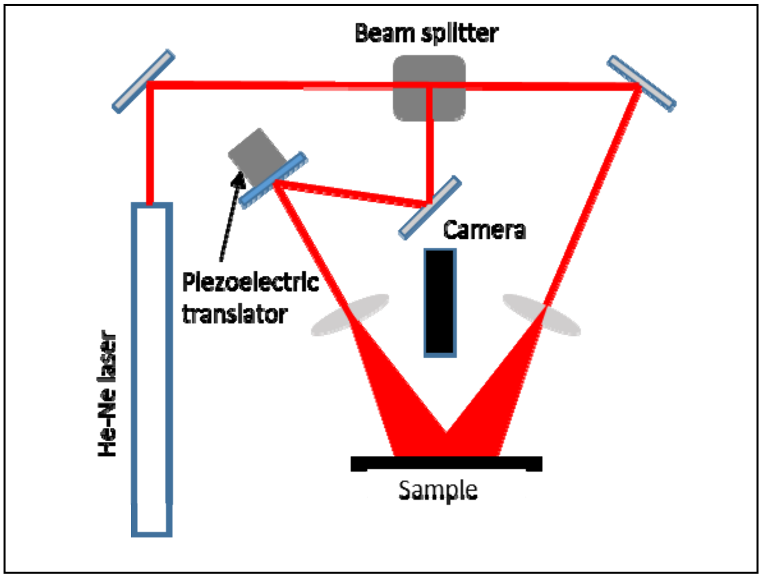

Figure 2. Electronic speckle pattern interferometry setup.

Computational methods

A realistic geometric model of the two weave architectures was constructed using Dynamic Fabric Mechanical Analyzer (DFMA) (see [2], [3]). This software models digital fibers as digital rod elements connected with flexible links and contact elements. The digital fibers are combined into yarns where all fibers have the same length. The volume occupied by one digital fiber would be filled by multiple actual fibers. One can then specify the number of digital fibers per yarn and whether the fibers in the yarn are straight or twisted. The yarns are assembled into an expanded representation of the unit cell topology and the final unit cell is determined from a dynamic relaxation approach. The surface of each yarn in the final structure is exported as a point cloud used to create the finite element mesh of the unit cell using a custom Matlab script. All model preparation steps are performed automatically within the MSC Mentat software using a custom Python script.

The volumetric mesh for the tows is generated using Marc Mentat based on the surface mesh for the yarns in the unit cell. The volumetric mesh for the resin is also generated in Marc Mentat by changing the sign of the normal vector to the surface mesh of the yarn. Custom scripts are used to modify the surface mesh at the lateral boundaries of the unit cell so that the mesh of the unit cell is periodic. More details of this process can be found in [4].

The properties of the RTM6 epoxy matrix are assumed to be homogeneous and isotropic. The modulus, E, and coefficient of thermal expansion, α, depend on temperature as:

$$\begin{aligned} E_m &= E_m^{0^o C} - \beta_m T \\ \alpha_m &= \alpha_m^{0^o C} + \gamma T \end{aligned} \qquad (1.1)$$

where $E_m^{0^o C} = 350\,MPa, \beta_m = 5.9\frac{MPa}{{}^o C}$, $\alpha_m^{0^o C} = 5\bullet 10^{-5}\frac{1}{K}$, *and* $\gamma_m = 1.05\bullet 10^{-7}\frac{1}{K}$ and T is in °C.

The yarns are modeled as a transversely isotropic material that represents the resin impregnated 12K carbon fibers assuming an 80% volume fraction of fibers within the yarns. The effective properties are estimated using micromechanical models of Hashin and Shapery [5], [6] for continuous unidirectional composites. as. E_{1t} = 221.38 GPa, E_{2t}= 13.18 GPa, $G1_{2t}$ = 7.17 GPa, v_{12t} = 0.35, v_{23t} = 0.35, α_{1t} = −2.29·10− 7 1/K , α_{2t} = 2.23·10−5. In these expressions, direction 1 is parallel to the axis of the yarn and directions 2 and 3 are transverse to the yarn axis. Note that even though the properties of the matrix in the tows change with temperature as given by (1.1), these changes will result in insignificant variations of the homogenized properties of the tows (see comparison in [7]), so in the numerical simulations the properties of the tows are assumed to be temperature independent.

The hole drilling was simulated using Marc Mentat's capability to deactivate elements. First, the simulation of the cooling after curing was performed assuming that the temperature of the completely cured composite panel uniformly changes from 185°C to 25°C while lateral surfaces of a unit cell stay periodic but are allowed to move laterally to accommodate the overall shrinkage of the composite panel. Then the elements corresponding to the position of the hole were manually selected to deactivate. Subtracting the displacements obtained after the simulation of curing from the displacements after removing the elements representing the hole produces the displacement field from the hole drilling.

RESULTS AND DISCUSSION

The location of the first hole we discuss is in the corner of the surface weft tow in the ply-to-ply (low constraint) architecture is shown in Figure 3. As can be seen from the images, the location of the actual hole is not precisely in the same location as the hole in the FE model.

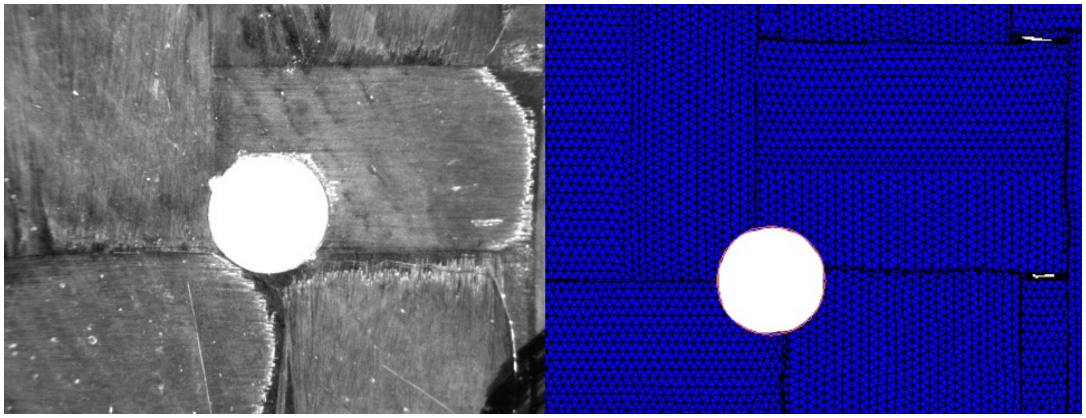

Figure 3. Location of hole in ply-to-ply structure for the data displayed in Figure 4. This hole is in the corner of a weft tow. The left hand image shows the location of the hole in the actual specimen and the right hand image shows the location in the finite element model. They are in slightly different locations.

The coordinate system was selected so that the weft direction is horizontal and the warp direction is vertical. The horizontal and vertical displacement fields as well as horizontal and vertical displacement slices for this location are shown in Figure 4. The top row shows the finite element prediction with a ±5 μm scale. The middle row shows the DIC results with a ±1 μm scale. The bottom row shows a horizontal slice through the horizontal displacement results and a vertical slice through the vertical displacement data.

The magnitude of the measured displacements is significantly lower than the predictions which strongly suggests that the level of intrinsic residual stress in the structure is significantly lower than predicted. The sign of the measured horizontal displacements is opposite in sign to the predicted displacements on the right hand side of the hole but closer in magnitude than the predicted displacements. The difference in model and actual hole location could explain the difference in the sign of the prediction. The sign and shape of the vertical displacement field is the same as the prediction but a factor of 2-3 lower than the predicted displacements. The displacements were measured by interferometry only for the horizontal displacements and the phase map (which is linearly proportional to displacement) is shown in Figure 5. The interferometry measurements compare well with the DIC measurements.

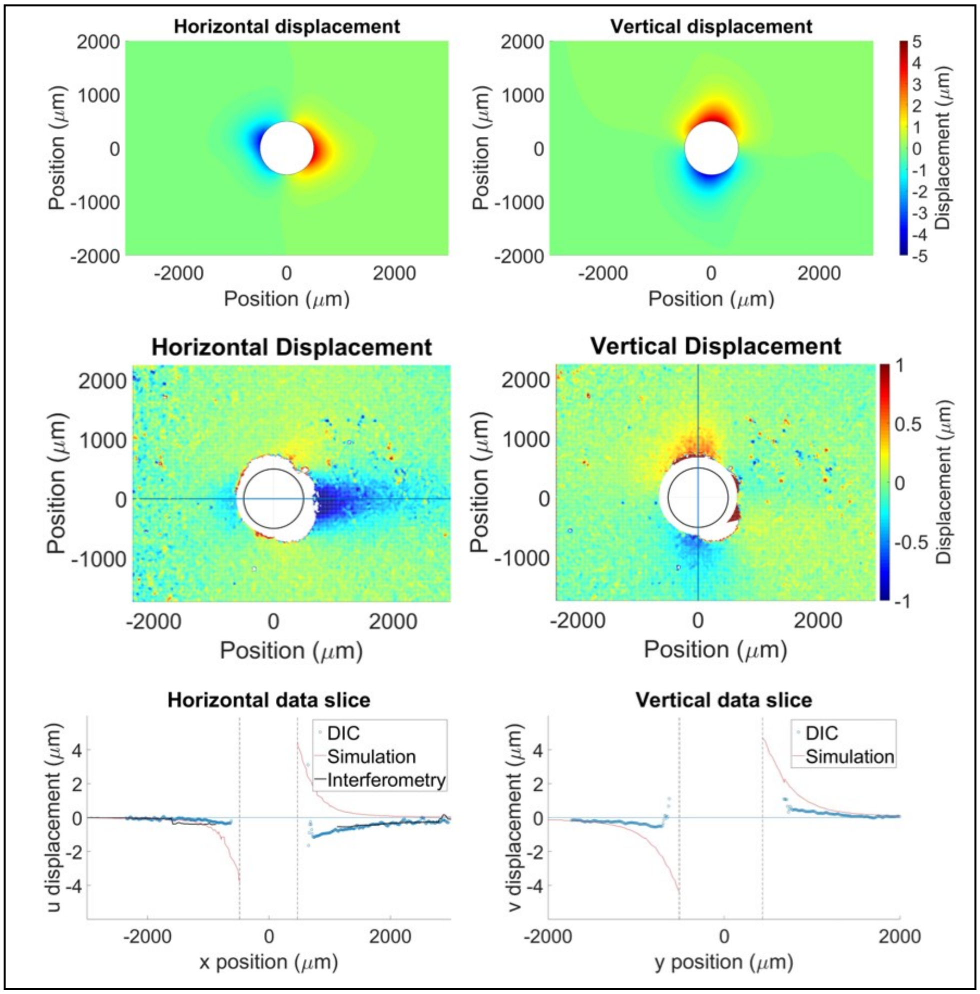

Figure 4. The top row shows the FE model prediction of horizontal and vertical displacement fields. The middle row shows the DIC measurements and the location of the slice plots on the bottom row.

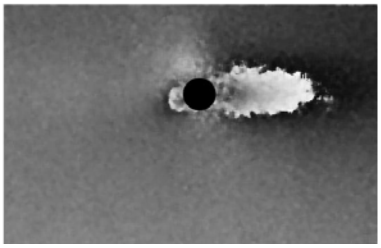

Figure 5. Phase map for horizontal displacements for Figures 3 and 4. Phase is encoded as a gray scale where white corresponds to a phase of 2π and black corresponds to zero. Phase is linearly proportional to displacement and one black-to-white transition is 449 nm of displacement.

The location of the second hole we discuss shown in Figure 6, is on the right hand side of a weft tow just above a warp tow in the ply-to-ply sample. The hole in the FE model is on the left side of the tow and is not precisely at the same location as the physical hole.

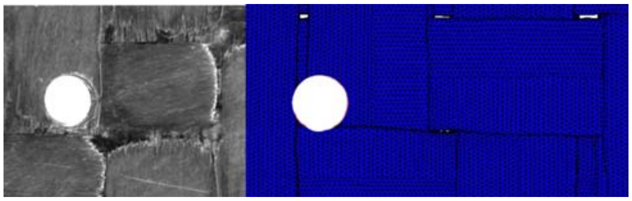

Figure 6. Location of hole in sample (left) and model (right) through a corner in the warp fiber in ply-to-ply structure. The holes are on opposite sides of the tow.

The set of displacement fields and slices for this hole shown in Figure 7 is organized similarly to the previous hole and uses the same, different magnitude displacement ranges for the displacement field plots. The sign of the both the horizontal and vertical displacement field for the prediction is opposite to that of both measurements. Again, this may be attributed to the difference in the placement of the hole. Future results will compare the same area. The magnitude of the measurements is a factor of 2-3 lower than the prediction of the FE model.

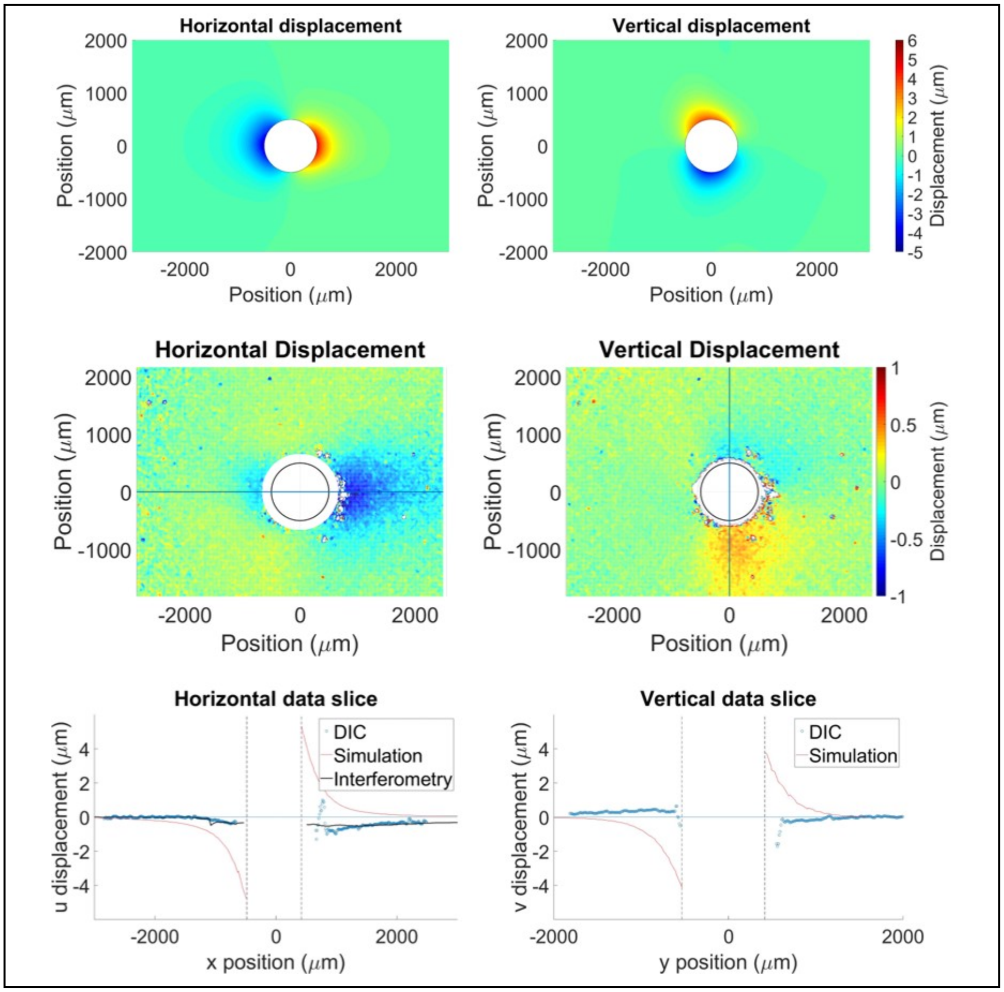

Figure 7. Model prediction (top row), DIC measurements, (middle row), and slice plots (bottom row) for the displacement fields in hole through warp tow shown in Figure 7,) through a corner in the warp fiber in ply-to-ply structure.

The location of the third hole is in between the warp and weft fibers in the orthogonal weave structure (which has more through-thickness constraint than the ply-to-ply structure) is shown in Figure 8. The actual hole and the model are very close to being in the same position.

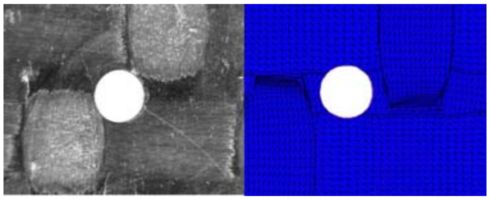

Figure 8. Location of hole in sample (left) and FE model (right) in between warp and weft tows in orthogonal weave architecture.

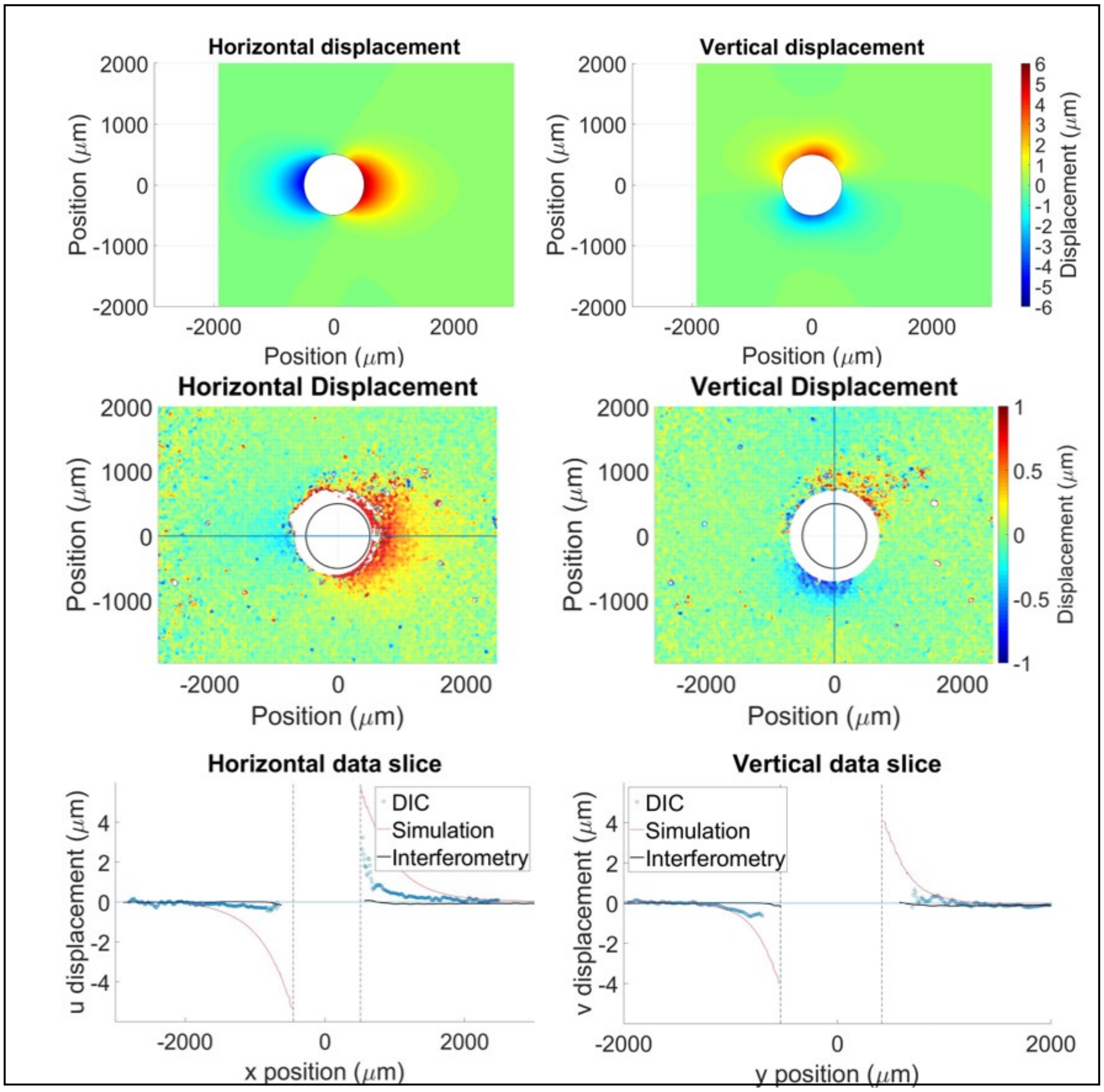

Figure 9. Model prediction (top row), DIC measurements, (middle row), and slice plots (bottom row) for the displacement fields in hole through warp tow shown in Figure 8, in between warp and weft tows in orthogonal weave architecture.

Again, the displacement fields follow the organization and magnitude convention of the previous images. The sign of the displacement fields is the same for the FE model and both the DIC and interferometric measurements. The magnitude of the measured displacements by DIC is generally smaller than the predictions but is sometimes very similar. The magnitude of the interferometric measurements is smaller than the DIC measurements and is smaller than the prediction.

The last hole we discuss is located near the center of a weft fiber in the orthogonal (high constraint) structure and is shown in Figure 10. The physical hole is closer to the center of the weft fiber than the hole in the model.

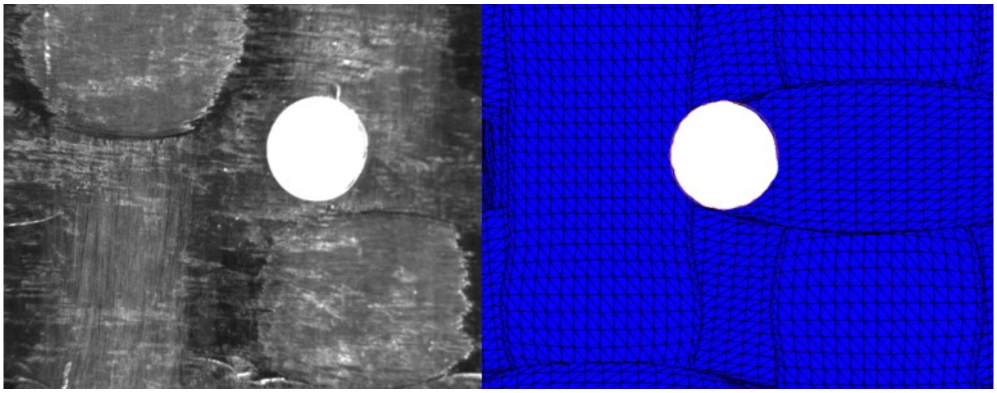

Figure 10. Location of hole in sample (left) and model (right) though a weft towr in the orthogonal structure.

The displacement fields and slices are shown in Figure 11. The sign of the horizontal displacement field is the same for the measurements and the model but is opposite for the vertical displacement. The magnitude of the horizontal displacements measured by DIC on the right side the hole is almost the same as for the model but the interferometric measurements are smaller.

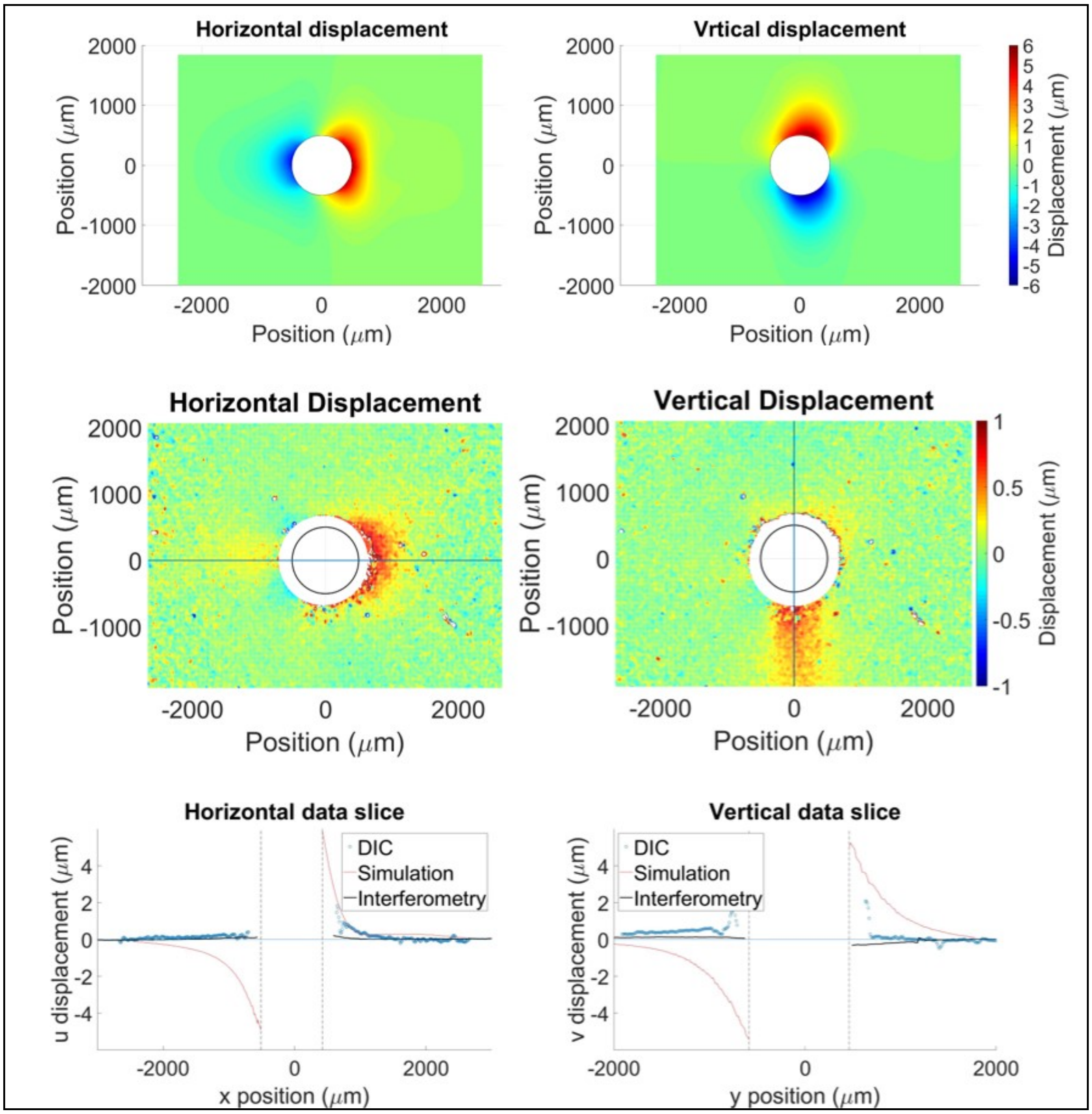

Figure 11. Model prediction (top row), DIC measurements, (middle row), and slice plots (bottom row) for the displacement fields in hole shown in Figure 10, in the center of a weft tow in the orthogonal weave architecture.

The interferometric horizontal and vertical displacement image pair for the hole in Figure 10 is shown in Figure 12. The relative displacements are as much as one full fringe which is equivalent to 0.449 μm of displacement. This is smaller than the model predictions and smaller than the DIC measurements.

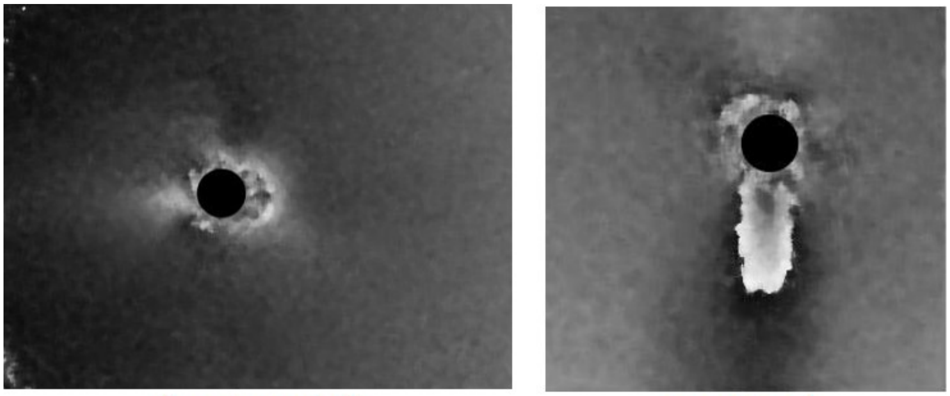

horizontal vertical

Figure 12. Interferometric phase maps for the horizontal and vertical displacements though the center of a weft tow in the orthogonal weave architecture. Phase is linearly proportional to displacement and one black-to-white transition is equivalent to 449 nm of displacement.

For most of the measurements, the observed displacements are smaller than the predicted displacements. This suggests that the magnitude of the intrinsic residual stress is smaller than the predicted stresses. This could be attributed to a number of factors including time dependent relaxation during cooling, differences in the actual hole location and the hole location in the model, or possibly the overcoat of epoxy that is in the model but not on the specimen. The differences in the sign of the displacements is likely due to the differences in position of the actual and modeled hole. We repeatedly re-evaluated the data to ensure that there was no unintended mirroring of the data. Future measurements and models will have holes that correspond more closely to one another.

The measured displacements were a pixel or less using DIC. Given that the resolution is no better than 0.01 pixel, the signal to noise is lower than desirable. Future DIC measurements will be conducted at double the magnification.

The pixel size in the interferometric measurement was 27 µm. This could lead to phase measurement errors in the high displacement gradient regions around the edge of the holes. Future measurements will be conducted at higher magnification.

ACKNOWLEDGEMENTS

This material is based upon work supported by the National Science Foundation through grant CMMI-1662098.

REFERENCES

[1] F. V Diaz, G. H. Kaufmann, and G. E. Galizzi, “Determination of residual stresses using hole drilling and digital speckle pattern interferometry with automated data analysis,” *Opt. Lasers Eng.*, vol. 33, no. 1, pp. 39–48, 2000.

[2] Y. Wang and X. Sun, “Digital-element simulation of textile processes,” *Compos. Sci. Technol.*, vol. 61, pp. 311–319, 2001.

[3] Y. Miao, E. Zhou, Y. Wang, and B. Cheeseman, “Mechanics of textile composites: microgeometry,” *Compos. Sci. Technol.*, vol. 68, pp. 1671–1678, 2008.

[4] A. Drach, B. Drach, and I. Tsukrov, “Processing of fiber architecture data for finite element modeling of 3D woven composites Dedicated to Professor Zdeněk Bittnar in occasion of his 70th birthday.,” *Adv. Eng. Softw.*, vol. 72, pp. 18–27, 2014.

[5] Z. Hashin, “Analysis of properties of fiber composites with anisotropic constituents,” *J. Appl. Mech.*, vol. 46, pp. 543–550, 1979.

[6] R.S. Schapery, “Thermal expansion coefficients of composite materials based on energy principles,” *J. Compos. Mater.*, vol. 2, pp. 380–404, 1968.

[7] B. Drach, I. Tsukrov, A. Trofimov, T. Gross, and A. Drach, “Comparison of stress-based failure criteria for prediction of curing induced damage in 3D woven composites,” *Compos. Struct.*, vol. 189, 2018.